Electronic Supplementary Material (ESI) for Materials Chemistry Frontiers.

Supporting Information for

Polymorphic Fluorescent Material with Strong Solid State Emission and Multi-Stimuli-Responsive Properties

Ji-Yu Zhu, Chun-Xiang Li, Peng-Zhong Chen, Zhiwei Ma, Bo Zou, Li-Ya Niu, Ganglong Cui* and Qing-Zheng Yang*

Methods and Materials

Unless otherwise noted, all chemical reagents and solvents were commercially available and were used without further purification. All reactions were monitored by thin layer chromatographic analysis on a pre-coated silica gel plate, which was visualized by a UV lamp at 254 or 365 nm. Flash column chromatography was performed on glass column of silica gel and solvent ratios were expressed in volume to volume. ^{1}H NMR spectra were recorded on a Bruker Avance 400 M spectrometer using tetramethyl silane (TMS) as internal standard at room temperature and referenced to the solvent signal. High resolution mass spectrometry (HR-MS) experiments were performed with Thermo Fisher Q-Exactive or Bruker Apex IV FTMS. UV−visible absorption and emission spectra for the solutions were recorded with Hitachi UV-3900 and F-4600 spectrometer, respectively. Fluorescence quantum yields were determined on Edinburgh instruments FLS-980 with an integrating sphere system. The values of lifetime were analyzed by exponential function fitting with software F900. Fluorescence microscope images were performed on OLYMPUS IXTI. Powder X-ray diffraction (PXRD) patterns were recorded at room temperature with a Shimadzu XRD-7000. Differential scanning calorimetry (DSC) analysis was performed in a Mettler Toledo DSC 1 instrument at heating and cooling rates of 10 °C /min under an N_2 atmosphere. The excitation source, a 355 nm line of a UV DPSS laser with the power of 4.5 mW, was used for PL measurements in situ high-pressure experiments. The images were obtained using a camera (Canon Eos 5D mark Ⅱ) equipped on a microscope (Ecilipse TI-U, Nikon). The in situ high-pressure absorption spectra were measured by a deuterium-halogen light source and recorded with an optical fiber spectrometer (Ocean Optics, QE65000).

Theoretical calculations

The starting geometric structures of compound **1** in different crystal forms are taken from crystal data in experiments. The unit cell is optimized at the Perdew−Burke−Ernzerhof level with periodic boundary conditions. The DNP basis set is used to expand the electronic wavefunction and the default dispersion correction is added to consider weak dispersion interactions. A Monkhorst−Pack k-point grid of 2 ×

2 × 2 is used. The DFT calculations are carried out by a DMol3 module that is integrated into the Materials Studio 2016 package.

A combined quantum mechanics/molecular mechanics (QM/MM) method consisting of central monomer (dimer) for the QM part and of surrounding molecules for the MM part is used to properly consider the crystal environment effect. The QM/MM calculation is realized with the ONIOM approach. In the ONIOM calculations the innermost molecule was treated using the accurate high-level quantum mechanics method, while the outermost molecules were treated using the efficient universal force field (UFF) method. The MM charges that were calculated using the QEQ formalism were embedded into the QM electronic structure. The B3LYP approach was chosen as the QM method for geometric optimizations in the S0 state while the TD-B3LYP approach was applied for geometric optimizations in the S1 states. In all DFT and TD-DFT calculations, the 6-31G* basis set was used for all the remaining atoms. In the ONIOM geometry optimizations, only the QM atoms were allowed to move in order to keep reasonable crystal structures. All the ONIOM geometry optimizations were carried out using the Gaussian09 package.

The natural orbitals for chemical valence (ETS-NOCV) approach was used to analyze the interactions between two fragments at the B3LYP/TZP level, with scalar relativistic effects being treated by the zeroth-order regular approximation (ZORA). Both fragment orbital analysis and the energy decomposition analysis were conducted at this computational level using the Amsterdam Density Functional (ADF2016) program.

Synthesis of 1

Compound **1** was synthesized according to the procedures reported in literatures [1-4].

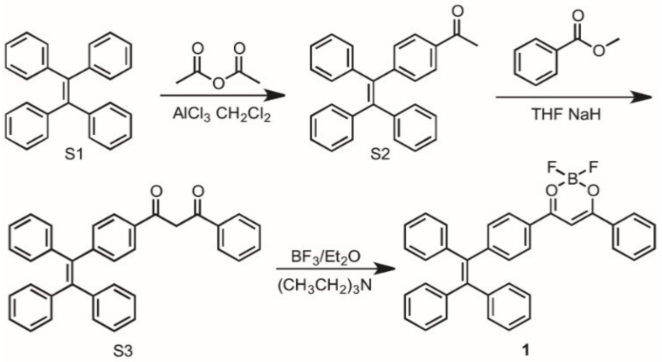

Scheme S1 Synthetic route of compound **1**

To a round-bottomed flask were added S1（3.8 mmol）in the slurry of $AlCl_3$ (11.4 mmol) and 15 mL anhydrous CH_2Cl_2 at room temperature. Acetic anhydride (4.18 mmol) dropwise by syringe pump was added to the reaction system. After stirring for 5 h, the reaction mixture was poured into H_2O (20 mL) and stirred for 0.5 h. The organic layer was collected and dried over anhydrous Na_2SO_4. After solvent evaporation under reduced pressure, the crude product was purified by column chromatography (silica gel, petroleum ether-ethyl acetate, v/v= 8 / 1) to obtain product **S2**. ^{1}H NMR (400 MHz, $CDCl_3$) δ 7.72 (d, *J* = 8 Hz, 2H) 7.25 -7.04 (m, 17H), 2.53 (s, 3H).

To a high-pressure tube was added compound S2 (2.0 mmol) in 5 mL anhydrous THF. The solution was purged with N_2 for 10 min, and then added NaH (57-63% oil dispersion, 25 mmol). After stirring for 30 min under N_2 at 65 °C, to the reaction mixture was added methyl benzoate (2.0 mmol). The reaction mixture was stirred for 24 hours at 65 °C under N_2 protection. After cooling to room temperature, the reaction was quenched by addition of water carefully in an ice bath. The pH was adjusted to 3 with HCl (aq). THF phase was separated, and the aqueous suspension was extracted with dichloromethane. The combined organic phase was dried over anhydrous Na_2SO_4, and concentrated under reduced pressure. The crude product was purified by column chromatography (silica gel, 4:1 v/v, petroleum ether/ethyl acetate) to afford product **S3** as yellow solid. Yield: 65 %.

To a stirring solution of compound S3 (2.00 mmol) in dry dichloromethane (5 mL) was added triethylamine (4.00 mmol) at room temperature. After 0.5 h, $BF_3·OEt_2$（2.29 mmol）was added and the reaction mixture was stirred for 12 h under no light condition. The solution was washed with 2 M HCl, saturated aqueous $NaHCO_3$, brine and dried over Na_2SO_4. After the solvent was removed by rotary evaporation, the residue was purified by column chromatography (silica gel, petroleum ether- CH_2Cl_2, v/v= 3 / 2) to afford 984.9 mg of target product **1** as bright orange solid. Yield: 84%.

^{1}H NMR (400 MHz, $CDCl_3$) δ 8.10 (d, *J* = 7.4 Hz, 2H), 7.89 (d, *J*= 8.5 Hz, 2H), 7.67 (t, *J* = 7.4 Hz, 1H), 7.53 (t, *J* = 7.8 Hz, 2H), 7.20 (d, *J* = 8.5 Hz, 2H), 7.17-7.09 (m, 10H), 7.06 -6.97 (m, 6H). ^{13}C NMR (101 MHz, $CDCl_3$) δ 182.6, 152.0, 144.0, 143.0, 143.0, 142.8, 139.6, 135.2, 132.2, 131.4, 131.4, 129.6, 129.3, 128.9, 128.6, 128.2, 128.2, 127.9, 127.5, 127.2, 127.2, 93.4.

Figure S1. The photograph of multipolymorphisms of compound **1** grown in dichloromethane/hexane mixed solution in the same bottle taken under UV irradiation at 365 nm.

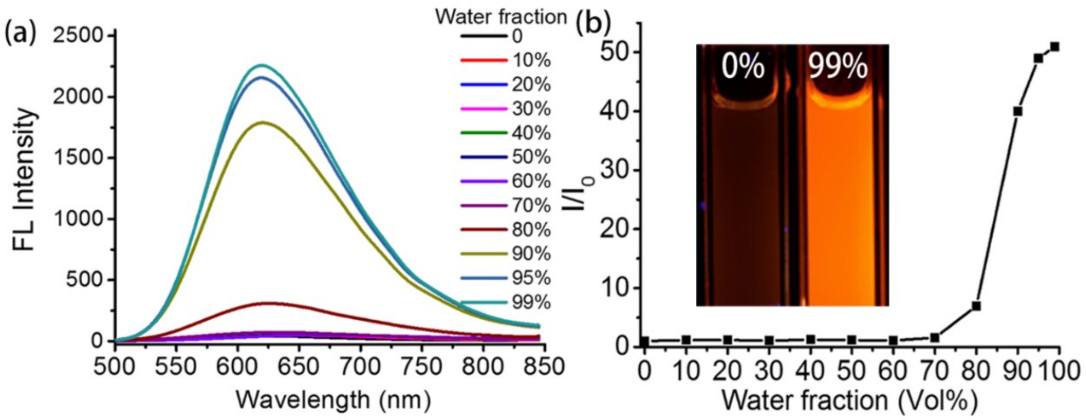

Figure S2. (a) Emission spectrum of compound **1** in THF–water mixtures with different water fractions at 50μM. λex = 420 nm. Normalized absorption spectrum of compound **1** in THF–water mixtures with different water fractions can be seen in the Figure S4 (Supporting Information). (b) Plot of I/I_0 versus water content of the solvent mixture, where I_0 is the emission intensity in the pure THF solution and photographs of compound **1** in the pure THF solution and the 99% water–THF mixture taken under illumination of a UV light. Compound **1** shows typical AIE property. Its weak emission at ca. 618 nm in THF solution keeps constant at mass fraction of water (fw) below 80%. Once more than 80% the emission intensity is gradually enhanced reaching a maximum at fw of 99% with ca. 50-fold enhancement (Figure b). This property is also seen under UV-lamp illumination.

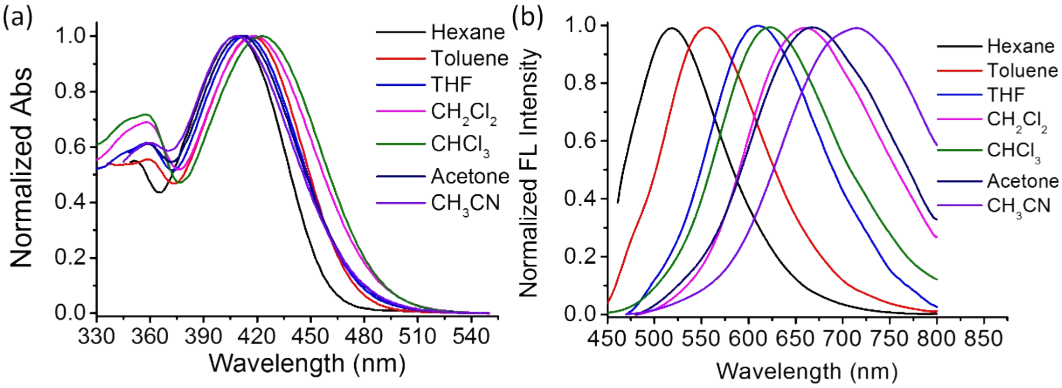

Figure S3. Normalized absorption (a) and emisssion spectra (b) of compound **1** in different solvents. $\lambda_{ex} = 420$ nm. Compound **1** was assigned to the ICT transition from the TPE unit to the dioxaborine ring. The absorption maximal in different solvents did not appear too much correlation with the polarity of solvents. In chloroform and dichloromethane, the compound showed the absorption spectra red shifted compared with that in other solvents. The emission bands became broad and red-shifted significantly with increasing polarity of the solvents, consistent with the strong ICT character of the solvent relaxed emissive state.

Table S1. Detailed photophysical properties of compound **1** in different crystal forms.

1	**state**	**λex** (nm)	**λem** (nm)	τ (ns)	ϕ (%)
1-G	pristine	420	520	1.75	49
	ground	433	618	6.44	45
	fuming	425	565	4.41	72
1-G'	pristine	415	520	2.21	46
	ground	433	620	5.71	41
	fuming	430	562	4.33	77
1-Y	pristine	432	557	4.24	75
	ground	433	619	5.34	43
	fuming	433	560	5.16	80
1-O	pristine	430	586	5.09	47
	ground	433	618	5.47	45
	fuming	434	565	4.71	77

Table S2. The torsion angles between different domains of compound **1**

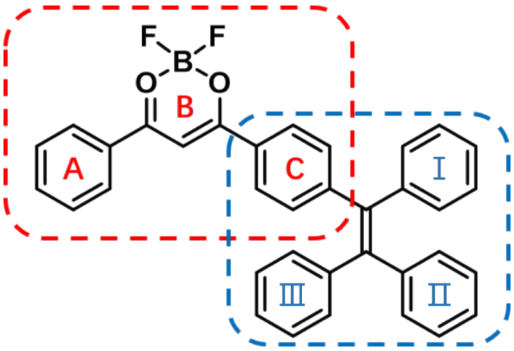

Torsion angle	**A&B**	**B&C**	**A&C**	**C& Ⅰ**	**C& Ⅱ**	**C&Ⅲ**
1−**G**	7. 21°	4.20°	11.35°	85.37°	80.71°	55.64°
1-G’	7.22°	6.18°	13.09°	86.45°	69.05°	58.59°
1-Y	30.31°	29.24°	52.45°	66.07°	89.40°	59.40°
1-O	26.47°	7.98°	34.45°	86.31°	63.45°	60.13°

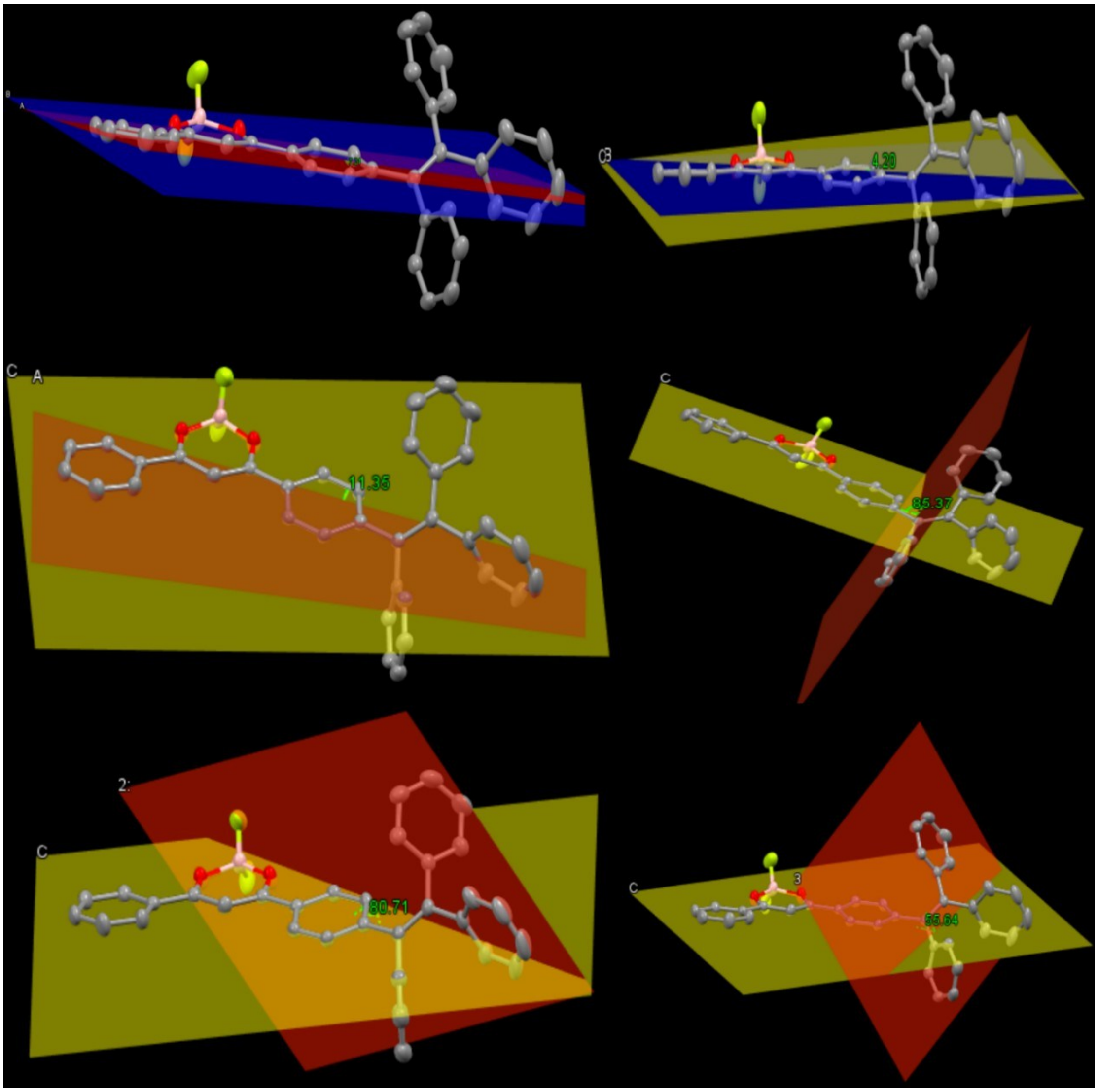

Figure S4. The torsion angles between different domains of 1-G: ring A &B, ring B&C (top line); ring A&C, ring C&Ⅰ(middle line); ring C&Ⅱ, ring C&Ⅲ(bottom line).

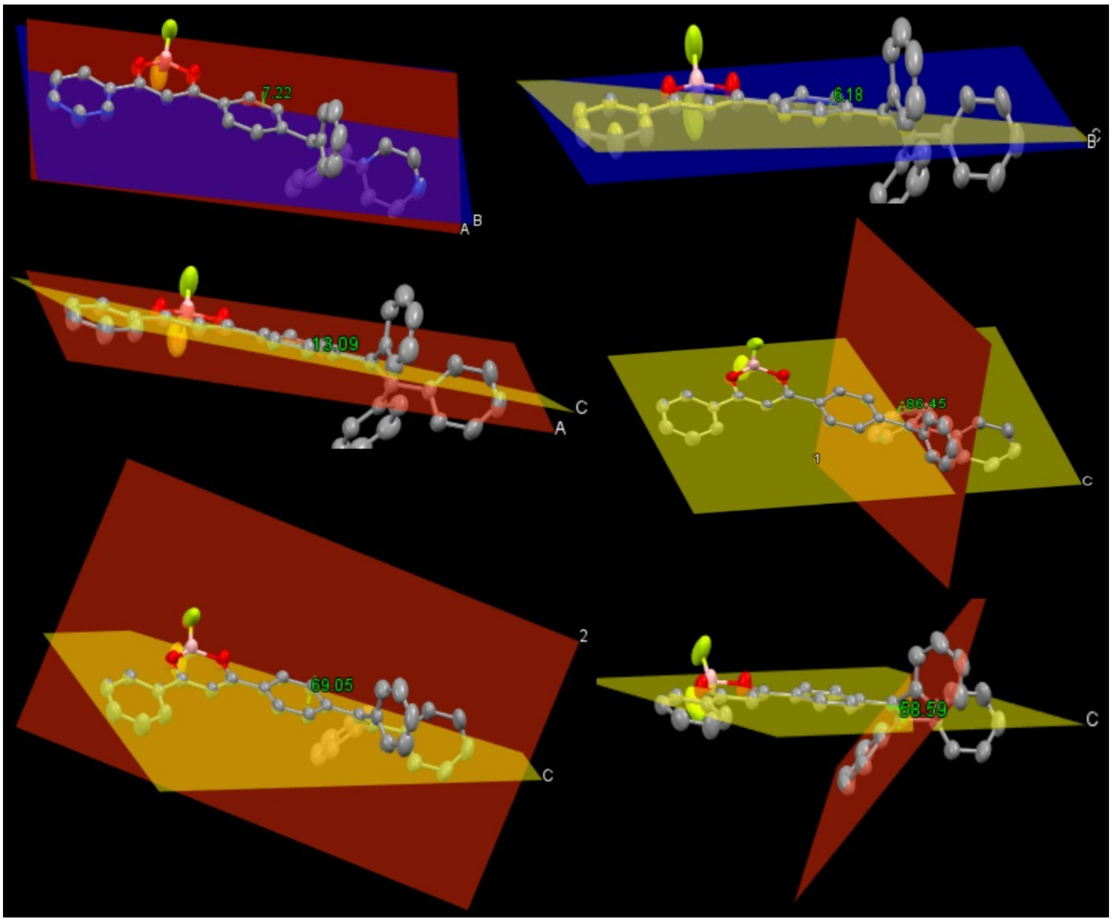

Figure S5. The torsion angles between different domains of 1-G’: ring A &B, ring B&C (top line); ring A&C, ring C&Ⅰ(middle line); ring C&Ⅱ, ring C&Ⅲ(bottom line).

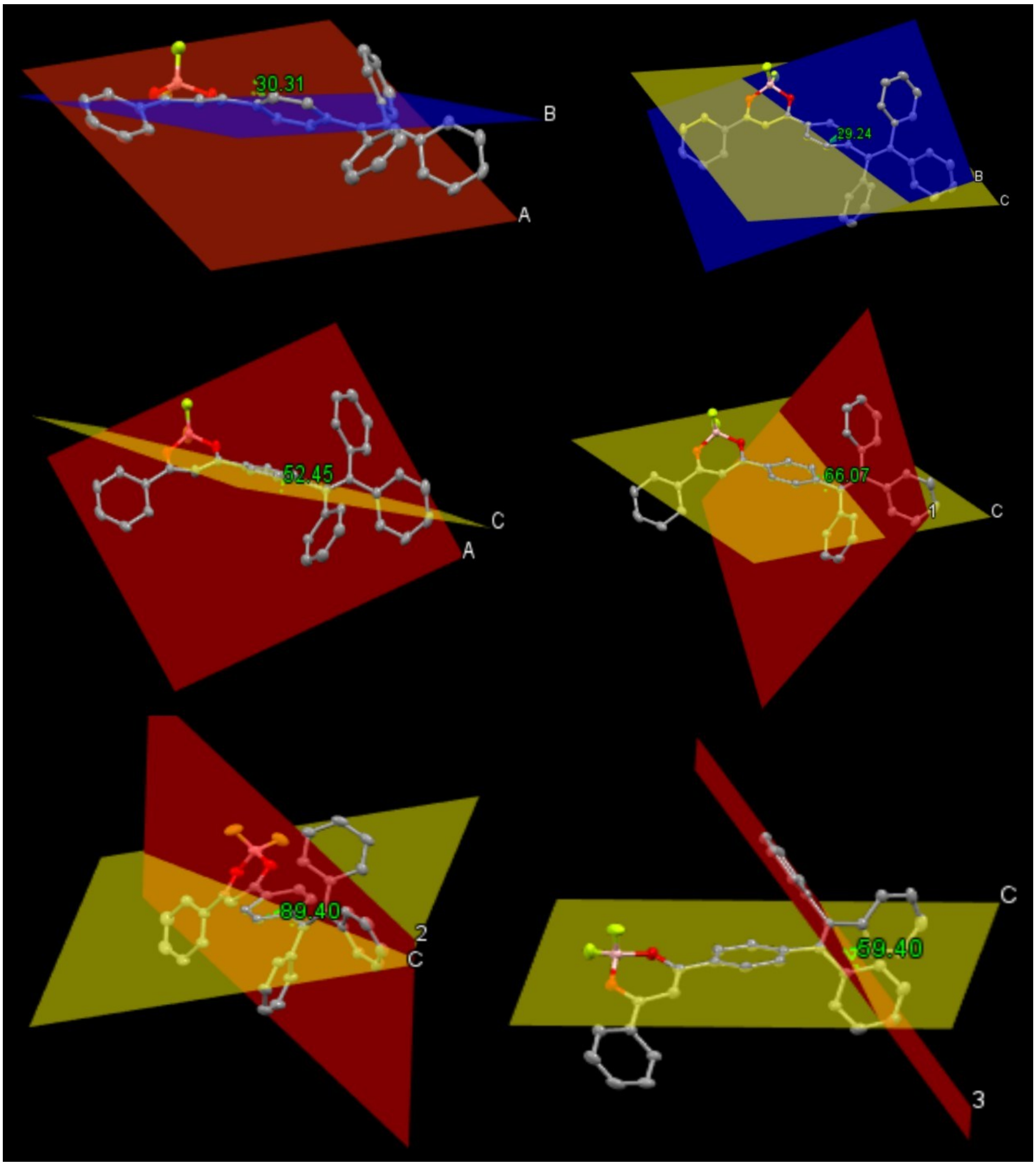

Figure S6. The torsion angles between different domains of 1-Y: ring A &B, ring B&C (top line); ring A&C, ring C&Ⅰ(middle line); ring C&Ⅱ, ring C&Ⅲ(bottom line).

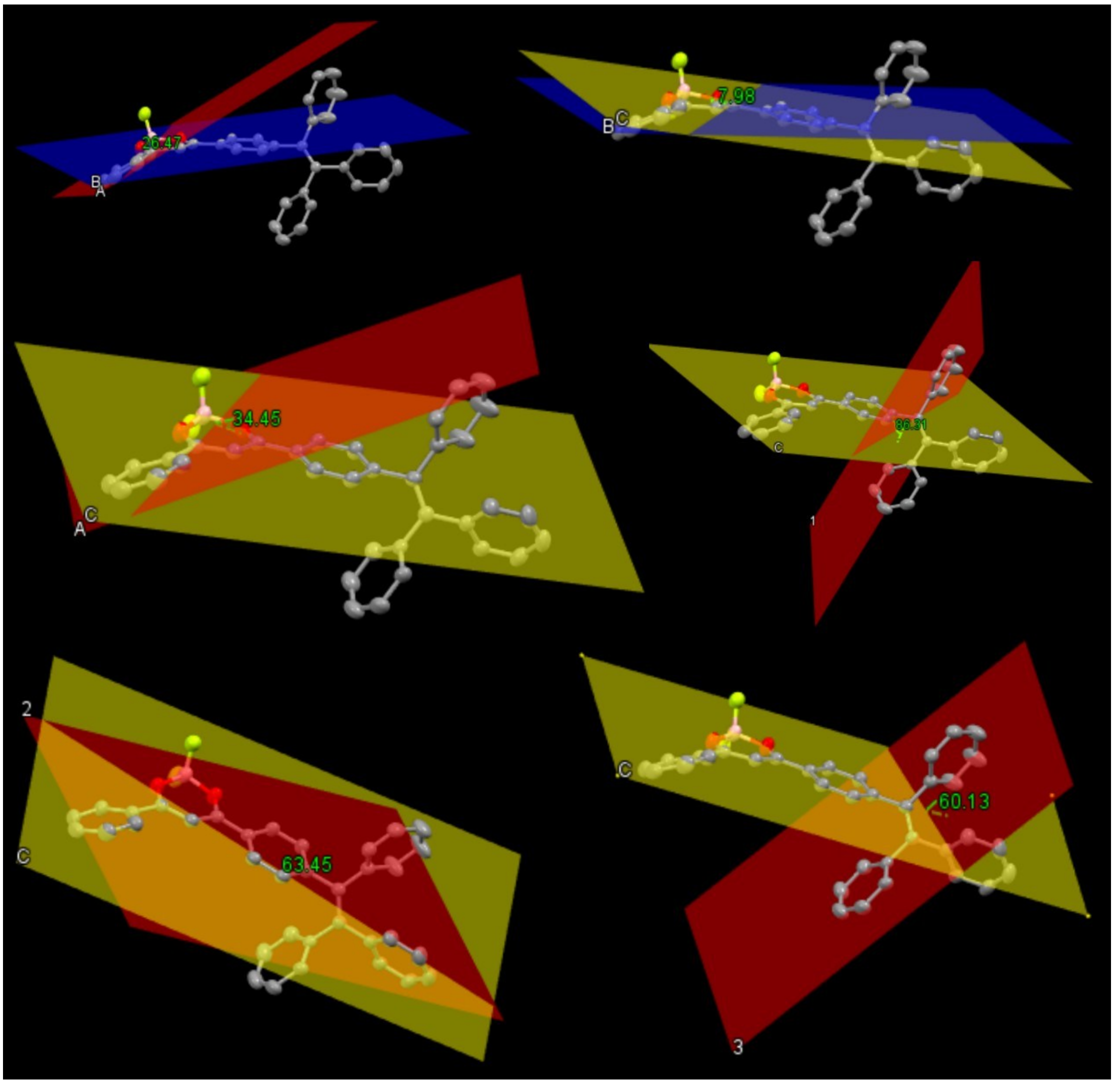

Figure S7. The torsion angles between different domains of 1-O: ring A &B, ring B&C (top line); ring A&C, ring C&Ⅰ(middle line); ring C&Ⅱ, ring C&Ⅲ(bottom line).

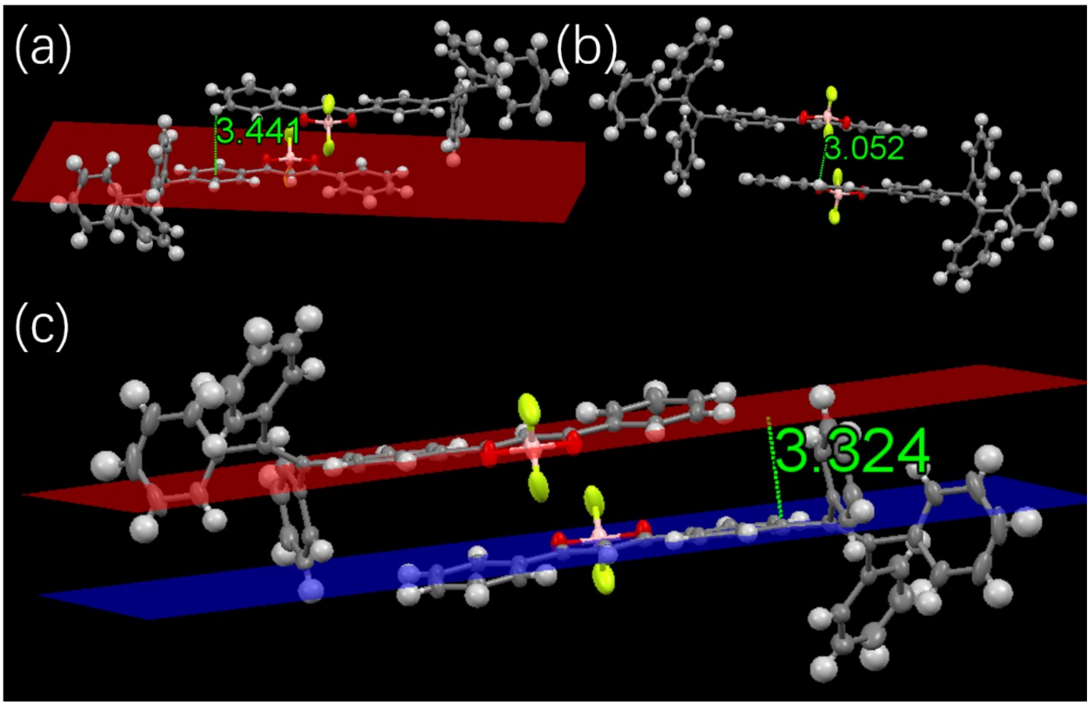

Figure S8. Multiple intermolecular interactions in 1-G such as dipole-dipole interactions, C–H...π (a), π–π stacking (b), and C–H...F hydrogen bonds (c, d) between adjacent molecules.

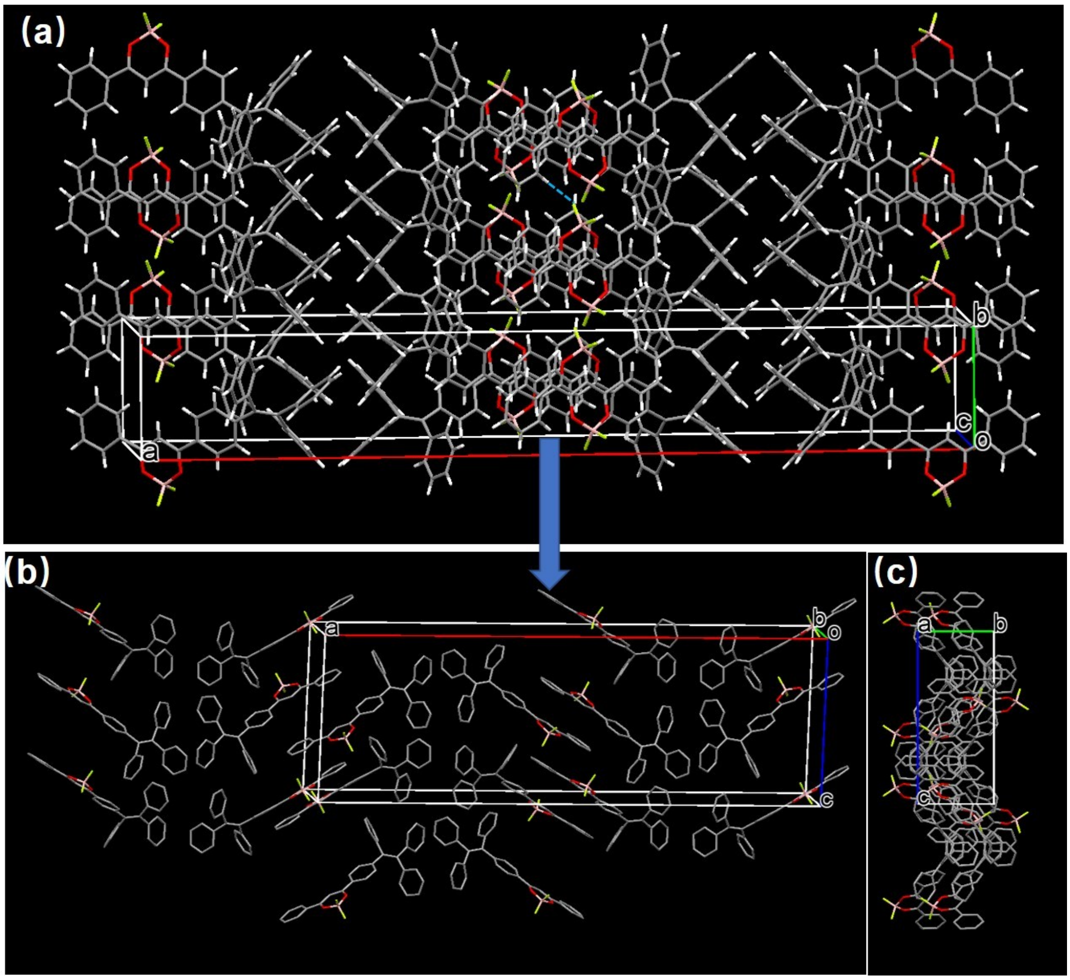

Figure S9. The molecular packing in the 1-G. (a) the molecular packing viewed along the c-axis direction. It indicates **1** formed layer structure which packs along the b-axis direction. (b) the molecular packing within each layer and viewed along the b-axis (b) and a-axis (c) directions

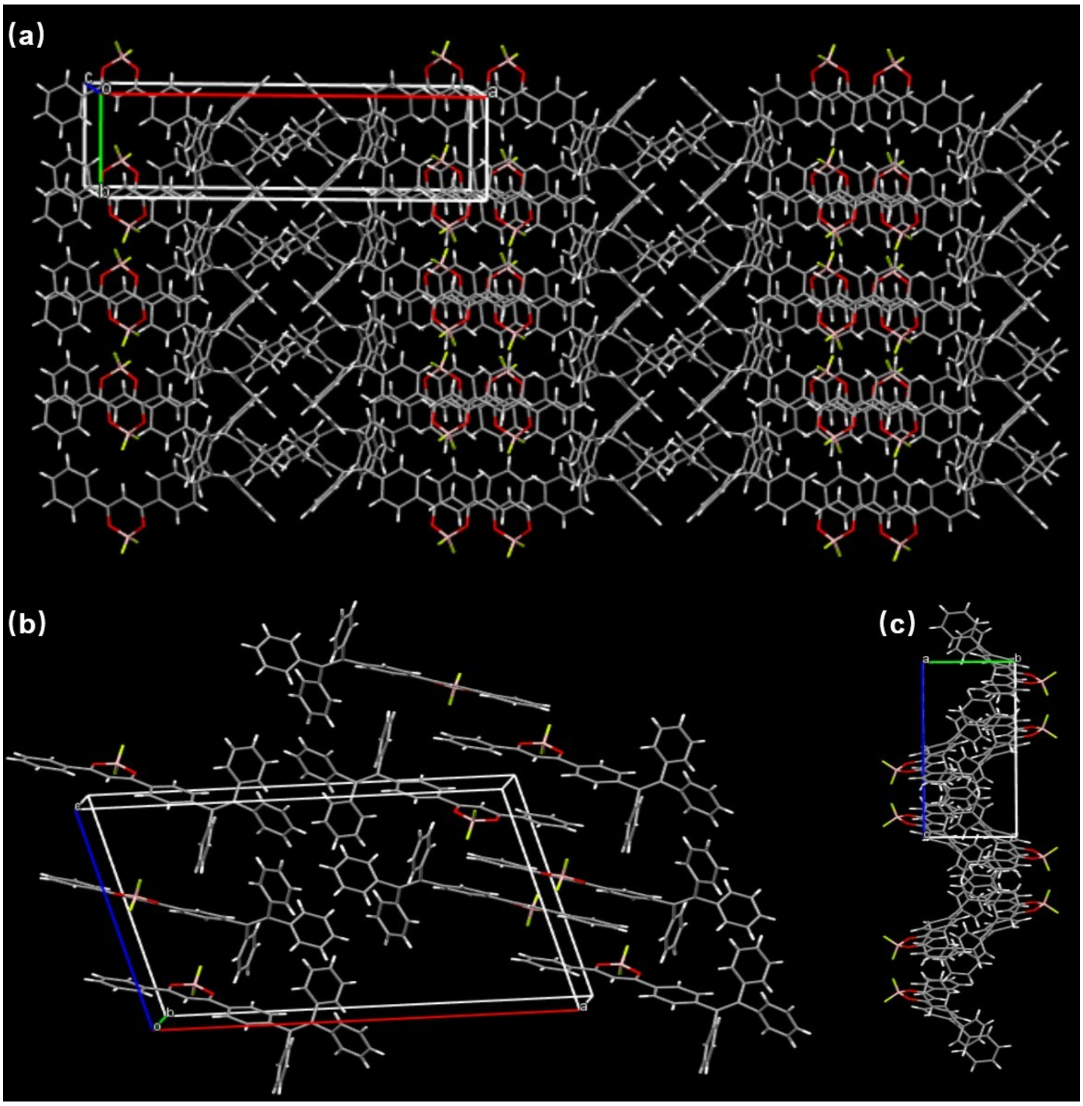

Figure S10. The molecular packing in the 1-G’. (a) the molecular packing viewed along the c-axis direction. 1-G’ also formed layer structure which packs along the b-axis direction. (b) the molecular packing within each layer and viewed along the b-axis (b) and a-axis (c) directions

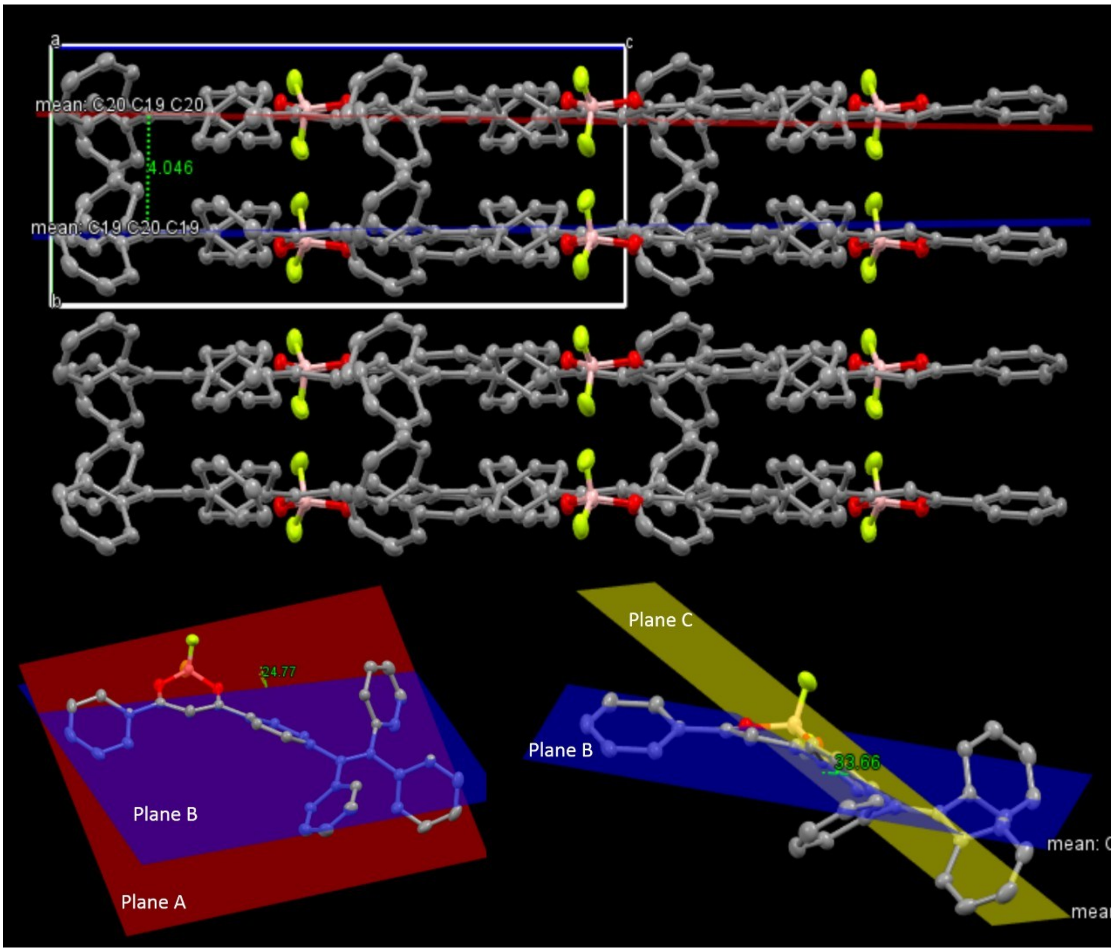

Figure S11. The molecular packing in the 1-Y. (a) the molecular packing viewed along the a-axis direction. It indicates **1** formed layer structure which packs along the b-axis direction. The interlayer distance of 4.05 Å. The molecules were overall flat in each layer while presenting mutual distortion among each component. (b, c) the molecular packing within each layer and viewed along the b-axis (b) and c-axis (c) directions

Table S3. Crystal data and structure refinement for 1-G

Indentification code	1-G	
Empirical formula	C35 H25 B F2 O2	
Formula weight	526.36	
Temperature	173 K	
Wavelength	1.54184	
Crystal system	orthorhombic	
Space group	Pbcn	
Uniti cell dimensions	a = 48.0265(13) Å	α = 90^0
	b = 7.1399(2) Å	β = 90^0
	c = 16.1674(6) Å	γ = 90^0
Volume	5543.9(3) Å^3	
Z	8	
Density(calculated)	1.261	
Absorption coefficient	0.694 mm-1	
F(000)	2192.0	
2Θ range for date collection	5.4140 to 75.8460^o	
Index ranges	-33 =< h =< 57, <5 =< k =< 8, -19 =< l =< 8	
Reflections collected	18780	
Indepent reflections	4820 (R_{int} = 0.0403, R_{sigma} = 0.0349)	
Absorption correction	multi-scan	
Max.& min. transmission	1.000 and 0.686	
Refinement method	Full-matrix least-squares on F_2	
Data/restraints/parameters	4820/0/361	
Goodness-of-fit on F^2	1.136	
Final R indices [I>2sigma(I)]	R1 = 0.0532, R2 = 0.1302	
R indices (all data)	R = 0.0723	

Table S4. Crystal data and structure refinement for 1-G’

Indentification code	1-G’	
Empirical formula	C35 H25 B F2 O2	
Formula weight	526.36	
Temperature	298 K	
Wavelength	1.54184	
Crystal system	Monoclinic	
Space group	P2/c	
Uniti cell dimensions	a = 24.5080(7) Å	α = 90^0
	b = 7.1148(2) Å	β = $101.430(3)^0$
	c = 16.4499(5) Å	γ = 90^0
Volume	2811.48(14) $Å^3$	
Z	4	
Density(calculated)	1.244 g/cm^3	
Absorption coefficient	0.684 mm-1	
F(000)	1096.0	
Crystal size	0.1, 0.08, 0.07	
2Θ range for date collection	3.5915-77.0856	
Index ranges	-30 =< h =< 30, -8 =< k =< 8, -19 =< l =< 20	
Reflections collected	16750	
Indepent reflections	4888 (R_{int} = 0.0522, R_{sigma} = 0.0520)	
Absorption correction	multi-scan	
Max.& min. transmission	1.000 and 0.305	
Refinement method	Full-matrix least-squares	
Data/restraints/parameters	4888/0/361	
Goodness-of-fit on F^2	1.040	
Final R indices [I>2sigma(I)]	R1 = 0.0486, R2 = 0.1492	

Table S5. Crystal data and structure refinement for 1-Y

Indentification code	1-Y	
Empirical formula	C35 H25 B F2 O2	
Formula weight	526.36	
Temperature	153 K	
Wavelength	1.54184	
Crystal system	orthorhombic	
Space group	$Pca2_1$	
Uniti cell dimensions	a = 15.781(3) Å	$\alpha = 90^0$
	b = 8.7539(18) Å	$\beta = 90^0$
	c = 19.382(4) Å	$\gamma = 90^0$
Volume	2677.6(9) $Å^3$	
Z	4	
Density(calculated)	1.306 g/cm^3	
Absorption coefficient	0.089 mm^{-1}	
F(000)	1096.0	
Crystal size	0.21 x 0.2 x 0.17 mm^3	
2Θ range for date collection	5.162^0 to 54.968^0	
Index ranges	-15 <= h <= 20,-10 <= k <= 11,-25 <= 1 <=15	
Reflections collected	10195	
Indepent reflections	4748[R_{int} = 0.0383, R_{sigma} = 0.0438]	
Absorption correction	multi-scan	
Refinement method	Full-matrix least-squares on F2	
Data/restraints/parameters	4748/1/361	
Goodness-of-fit on F^2	1.143	
Final R indices [I>2sigma(I)]	R_1 = 0.0472, wR_2 = 0.1315	

Table S6. Crystal data and structure refinement for 1-O

Indentification code	1-O	
Empirical formula	C35 H25 B F2 O2	
Formula weight	526.36	
Temperature	153 K	
Wavelength	1.54184	
Crystal system	tetragonal	
Space group	$P4_32_i$	
Uniti cell dimensions	a = 11.2434(16) Å	$\alpha = 90^0$
	b = 11.2434(16) Å	$\beta = 90^0$
	c = 44.141(9) Å	$\gamma = 90^0$
Volume	5580.1(19) $Å^3$	
Z	8	
Density(calculated)	1.253 g/cm^3	
Absorption coefficient	0.085 mm^{-1}	
F(000)	2192.0	
Crystal size	0.24 x 0.21 x 0.20 mm^3	
2Θ range for date collection	3.69^0 to 52.724^0	
Index ranges	-14 <= h <= 14,-9 <= k <= 14,-50 <= l <=52	
Reflections collected	34409	
Indepent reflections	5605[R_{int} = 0.0438, R_{sigma} = 0.0248]	
Absorption correction	multi-scan	
Refinement method	Least Squares minimisation	
Data/restraints/parameters	5605/0/361	
Goodness-of-fit on F^2	1.218	
Final R indices [I>2sigma(I)]	R_1 = 0.0493, wR_2 = 0.1555	

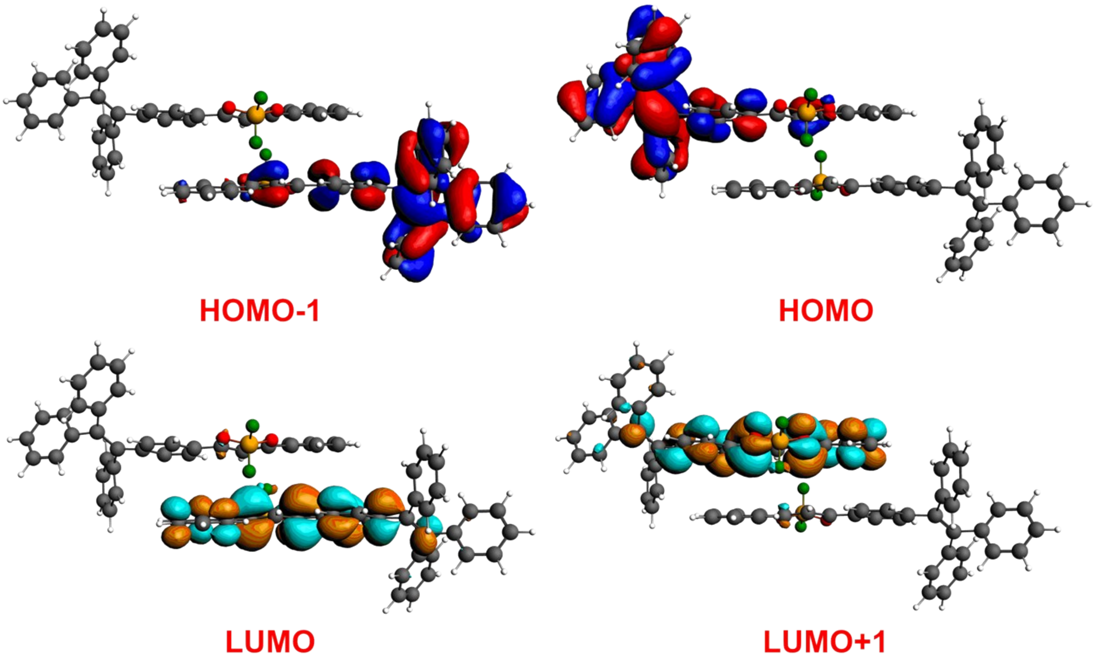

Figure S12. Frontier molecular orbitals (HOMO, HOMO-1, LUMO, and LUMO+1) of the dimer structures of 1-G’ in its S_1 minima.

Table S7. TD-DFT calculated vertical emission energies in nm, oscillator strengths, characters, and experimental values for 1-G, 1-G’ 1-Y and 1-O crystals.

	exp. nm	**Theo. nm**	**oscillator str.**	**Character**
1-G	520	533	0.0938	HOMO-LUMO
1-G’	520	536	0.0607	HOMO-LUMO
1-Y	565	555	0.4357	HOMO-LUMO
1-O	586	581	0.0410	HOMO-LUMO

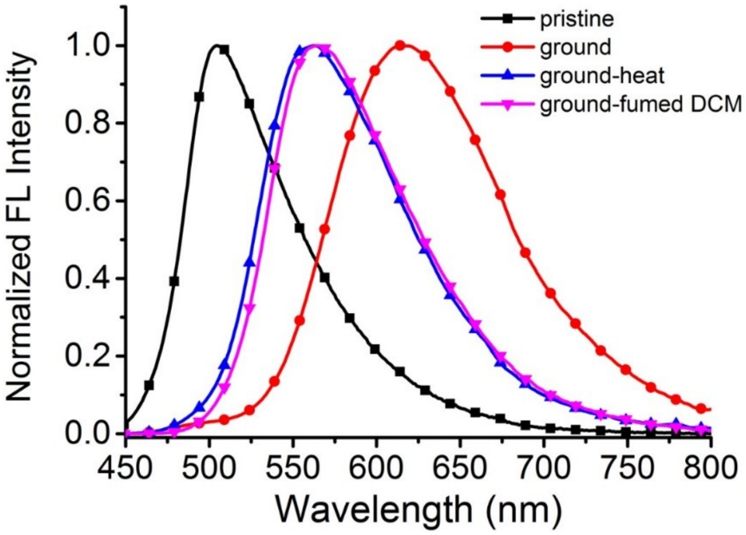

Figure S13. Normalized emission spectrum of 1-G' as pristine crystalline powders (black line), ground for 10 min (red line), heated at 220 ^{o}C for 30 min after ground (blue line), and fumed with DCM vapor for 2 min after ground (pink line). $\lambda_{ex} = 420$ nm.

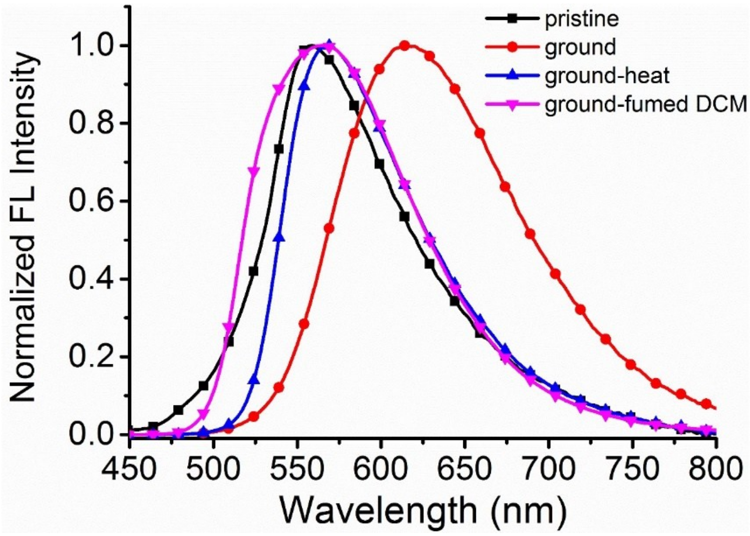

Figure S14. Normalized emission spectrum of 1-Y as pristine crystalline powders (black line), ground for 10 min (red line), heated at 220 °C for 30 min after ground (blue line), and fumed with DCM vapor for 2 min after ground (pink line). λ_{ex} = 420 nm.

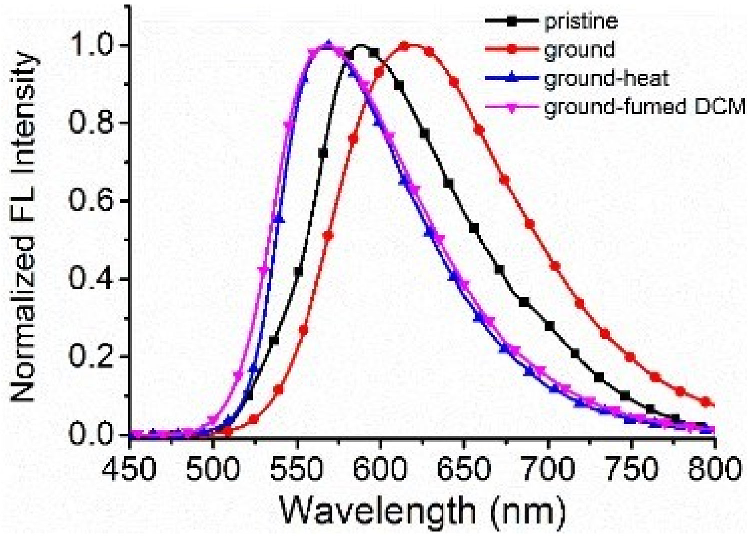

Figure S15. Normalized emission spectrum of 1-O as pristine crystalline powders (black line), ground for 10 min (red line), heated at 220 °C for 30 min after ground (blue line), and fumed with DCM vapor for 2 min after ground (pink line). λ_{ex} = 420 nm.

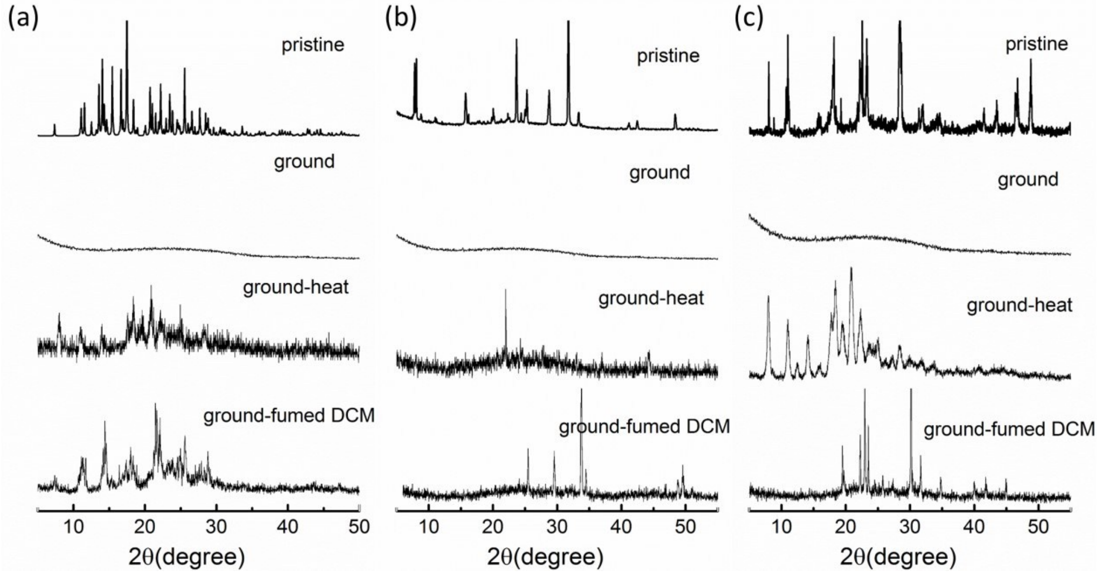

Figure S16. The Powder X-ray diffraction (PXRD) patterns of crystals of 1-G(a), 1-Y (b) and 1-O (c) in pristine, ground, ground-heat and ground-fumed DCM states. The PXRD of all crystalline powder manifested intense and sharp peaks, whereas the broad and featureless reflections were observed for ground samples (1-R), indicating that grinding resulted in a change of the molecular packing from crystalline state to amorphous state. After the ground samples were annealed at 220 ^{o}C for 30 min, PXRD of annealed samples manifested sharp peaks which were similar to the peaks of the pristine 1-Y crystal. Heating the ground samples induced the conversion from amorphous to 1-Y crystalline state rather than1-G or 1-O crystalline states, suggesting that 1-Y crystalline state was more thermodynamic stable than other states. In addition, the PXRD patterns of the samples fumed with dichloromethane vapor for 10 minutes after fully ground exhibted sharp peaks which were similar to pristine 1-Y , indicating the transformation from amorphous to 1-Y.

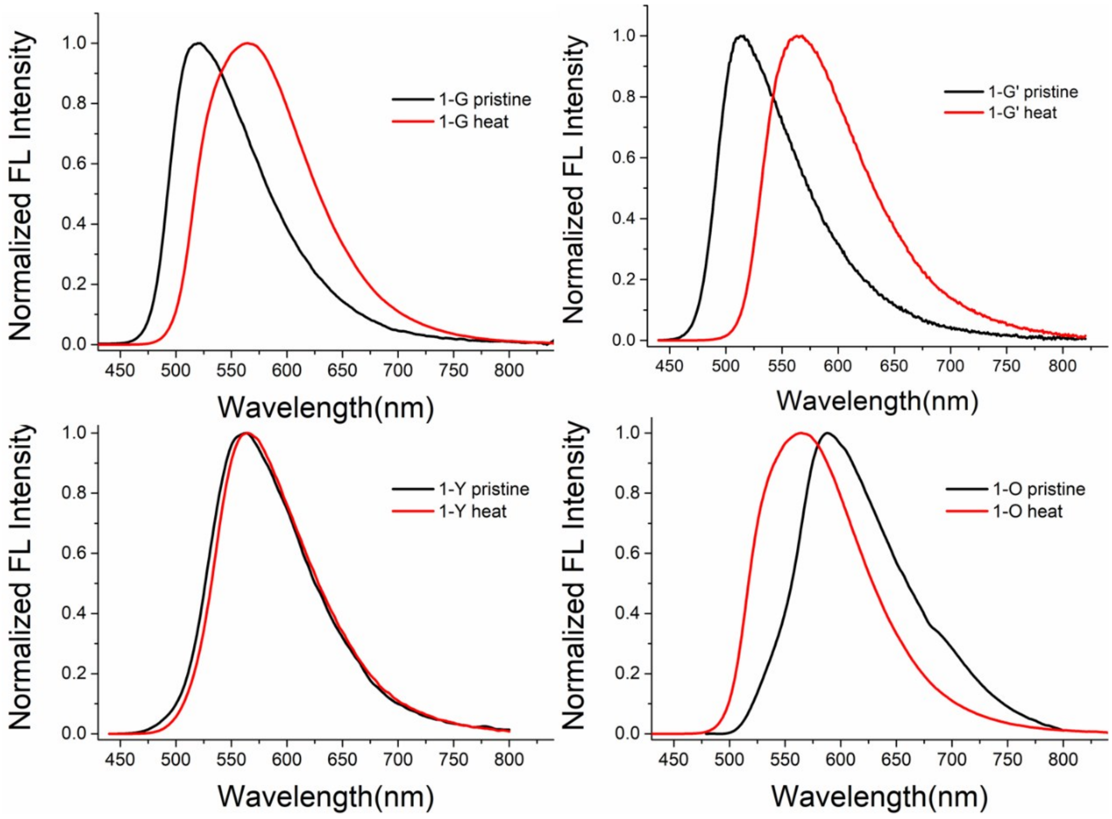

Figure S17. Normalized emission spectra of 1-G, 1-G**'**, 1-Y and 1-O as pristine crystalline powders (black line) and heated at 220 °C for 30 minutes (red line). λ_{ex} = 420 nm.

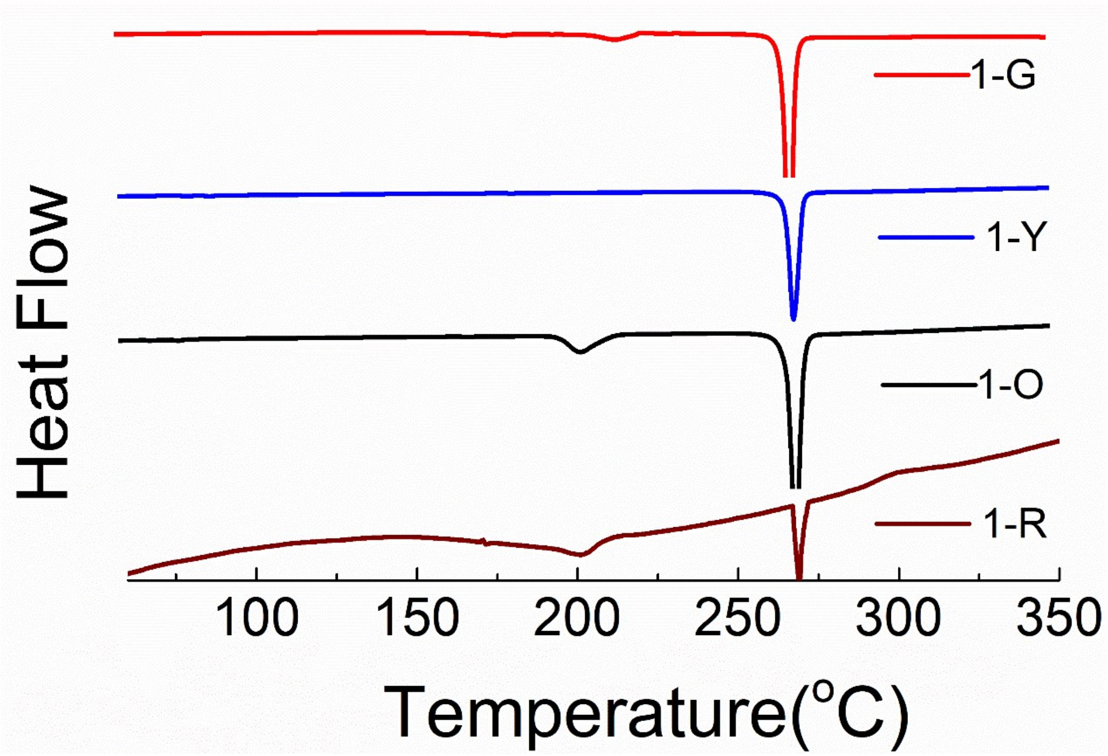

Figure S18. DSC curves of 1-G, 1-Y, 1-O crystal samples and 1-R amorphous sample, respectively. All crystal curves exhibited the same strong endothermic peak at 270 °C, which corresponded to their melting point. Meanwhile, the other endothermic peak was observed in the DSC curves of 1-G and 1-O at 204 °C and 218 °C (the black circle), respectively. It indicated the heating process involved a crystalline- crystalline transformation. (1-G' crystal sample was not enough to get DSC curve.)

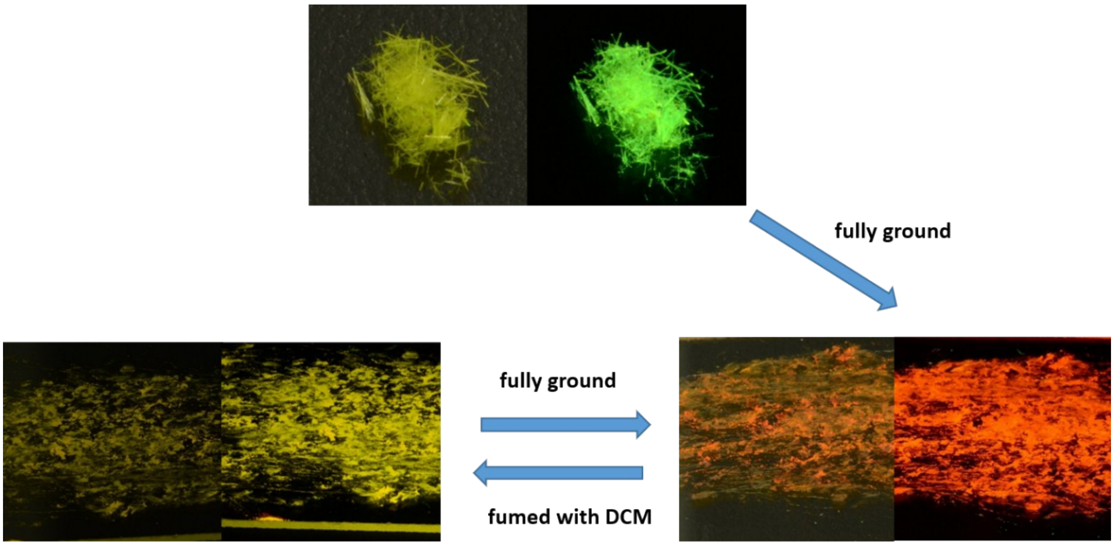

Figure S19. Transition of the1-G crystal with diverse luminescent colors upon stimuli: the 1-G pristine crystal (top) can transform into the 1-R aggregates (bottom right) by fully grinding; the pristine state (top) also can transform into the 1-Y crystalline powders(bottom left) by heating at 220 ^{o}C for 30 minutes or fuming with DCM vapor for 10 minutes; the amorphous aggregates also can transform into the 1-Y crystalline powders by fuming with DCM vapor for 10 minutes. The photographs were taken in sunshine in the left column of every group, the photographs of the right column were taken under UV irradiation at 365 nm in every group.

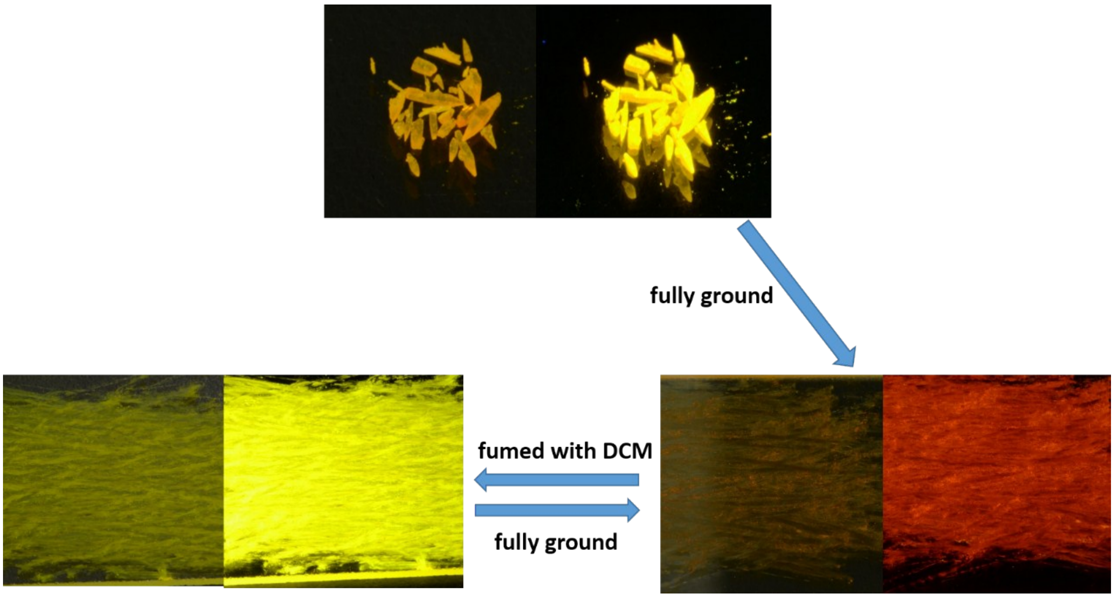

Figure S20. Transition of the 1-Y crystal with diverse luminescent colors upon stimuli: the 1-Y pristine crystal (top) can transform into the 1-R aggregates (bottom right) by fully grinding; the amorphous aggregates can revert to the pristine 1-Y crystalline powders by fuming with DCM vapor for 10 minutes. The photographs were taken in sunshine in the left column of every group, the photographs of the right column were taken under UV irradiation at 365 nm in every group.

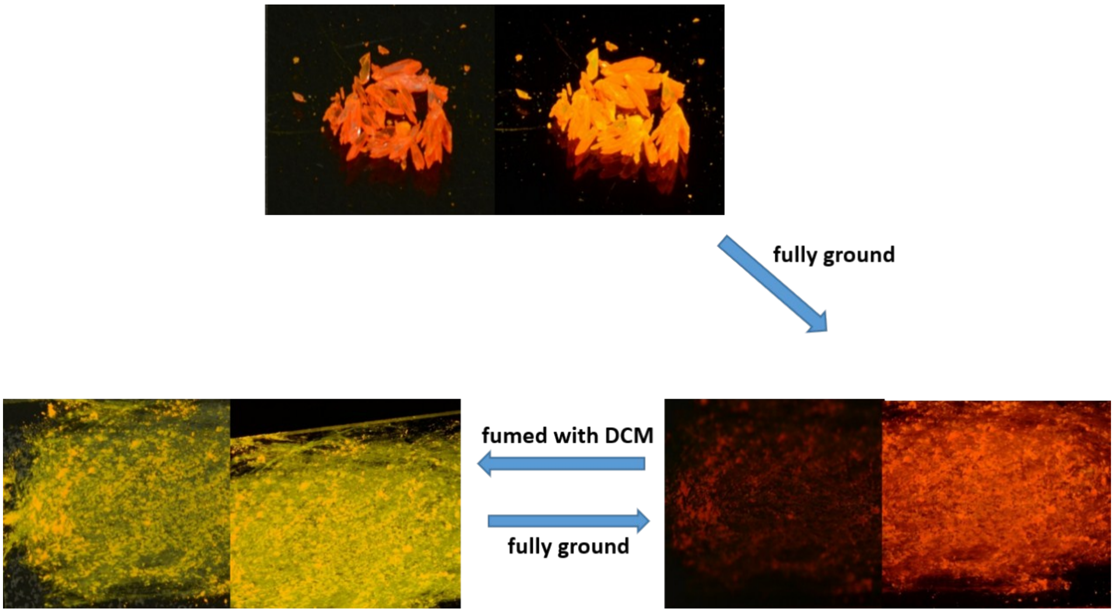

Figure S21. Transition of the 1-O crystal with diverse luminescent colors upon stimuli: the 1-O pristine crystal (top) can transform into the 1-R aggregates (bottom right) by fully grinding; the pristine state (top) also can transform into the 1-Y crystalline powders(bottom left) by heating at 220 °C for 30 minutes or fuming with DCM vapor for 10 minutes; the amorphous aggregates also can transform into the 1-Y crystalline powders by fuming with DCM vapor for 10 minutes. The photographs were taken in sunshine in the left column of every group, the photographs of the right column were taken under UV irradiation at 365 nm in every group.

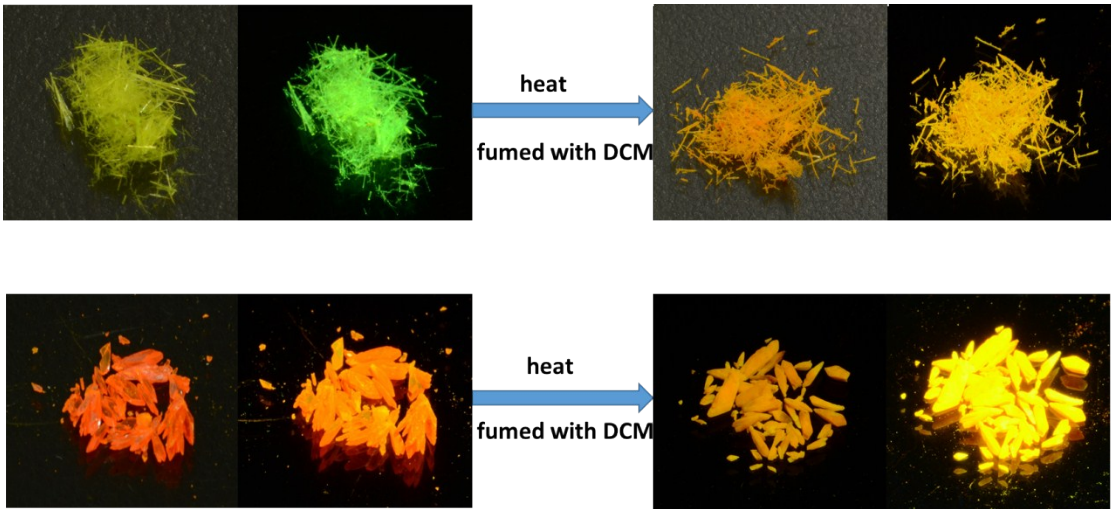

Figure S22. Transition of the 1-G and 1-O crystals with diverse luminescent colors under heating at 220 ^{o}C for 30 min: after heating at 220 ^{o}C for 30 min, both the 1-G (top) and 1-O (bottom) crystalline powders turned from the their initial green and orange emission into yellow (1-Y) at 560 nm . The photographs were taken in sunshine in the left column of every group, the photographs of the right column were taken under UV irradiation at 365 nm in every group.

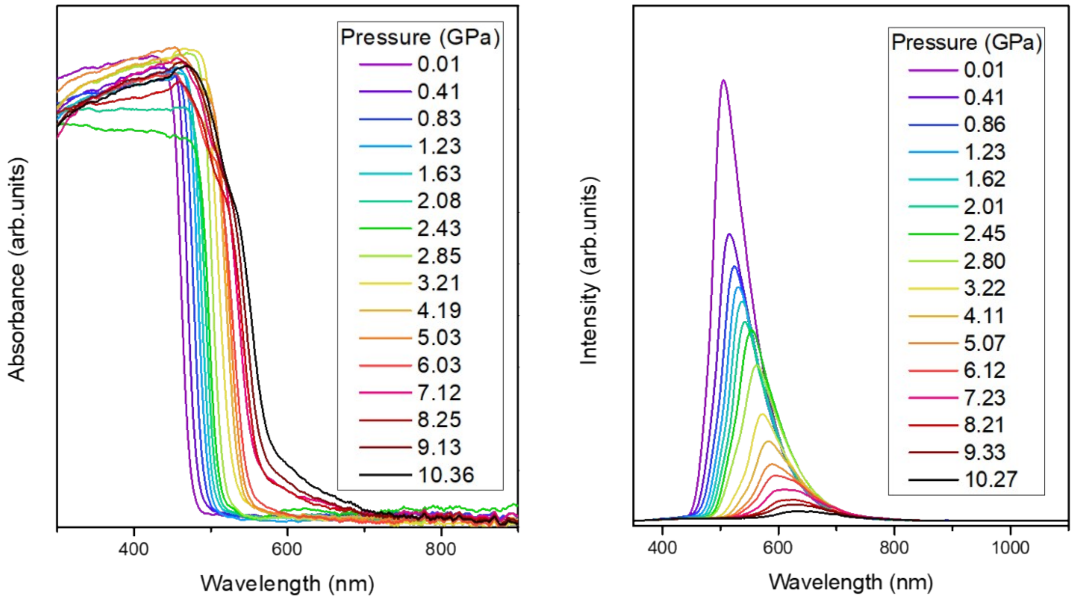

Figure S23. The situ absorption (left) and emisssion (right) spectra of 1-G under different pressures. The emission color of the crystal gradually shifted from green (520 nm) to yellow (574 nm), and eventually to red (651 nm), along with a monotonic decrease in intensity. The red shift was ascribed to the pressure-induced decrease of intermolecular distances and revolving of the molecular planes It was confirmed by the gradually broad and red-shifted absorption spectra with increment of pressure. The emission signal was fully quenched at the pressure of 10.36 GPa.

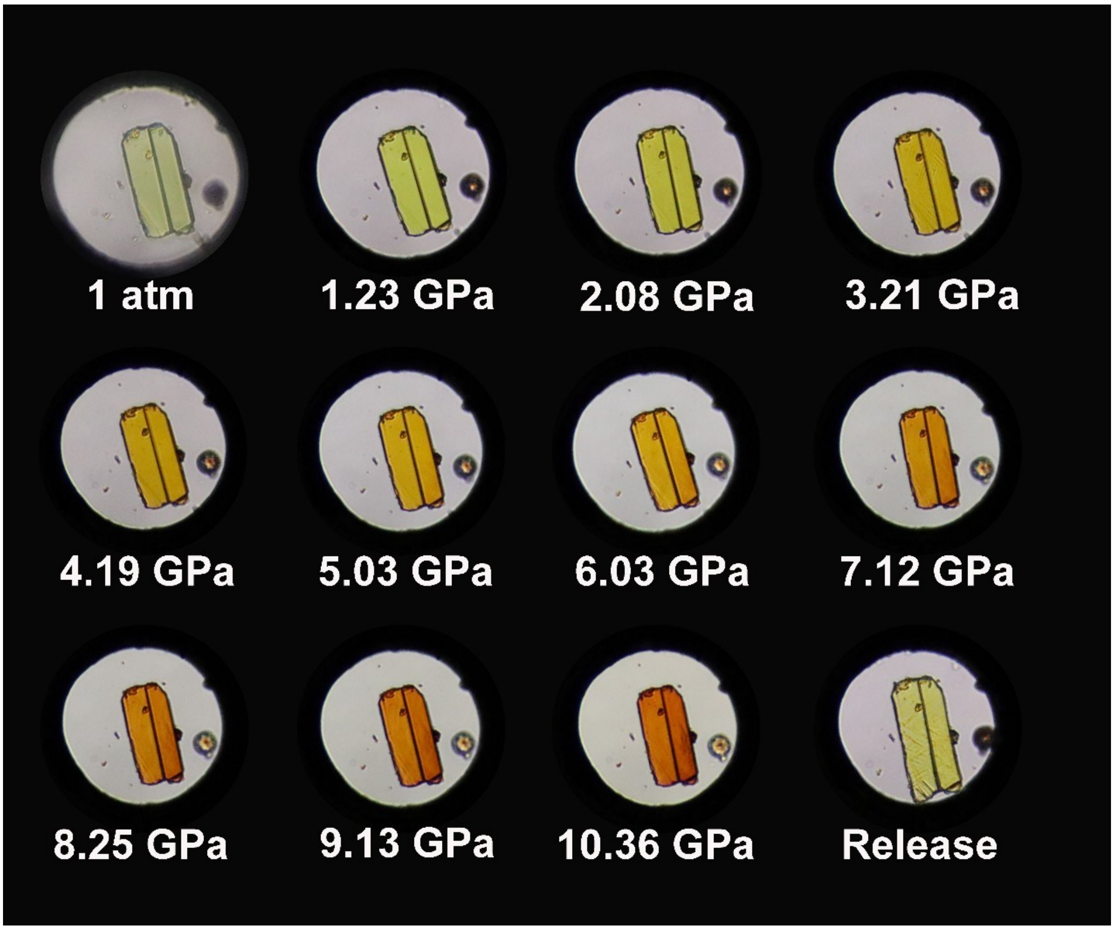

Figure S24. The situ absorption images of 1-G under different pressures under daylight.

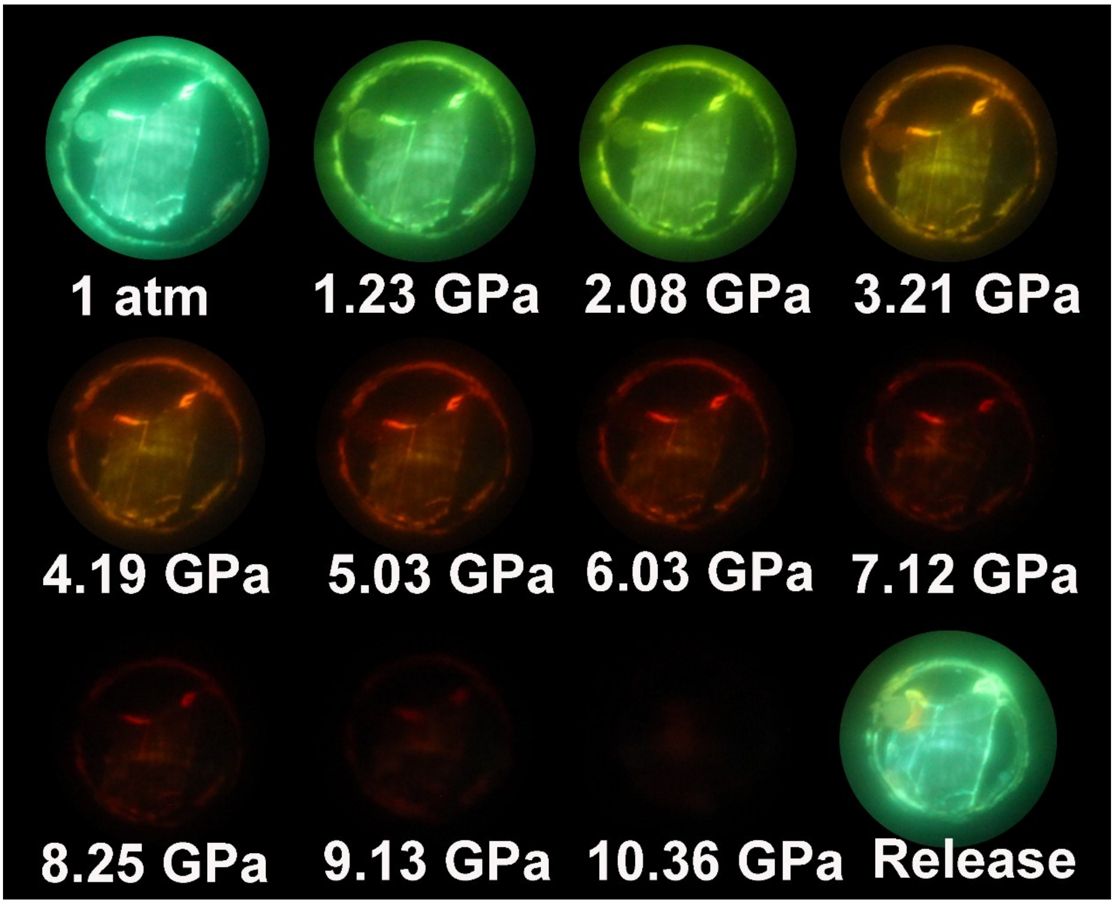

Figure S25. The situ fluorescense images of 1-G under different pressures. The images were obtained using a camera (Canon Eos 5D mark Ⅱ) equipped on a microscope (Ecilipse TI-U, Nikon).The carema can record the photographs under the same conditions including exposure time and intensity.

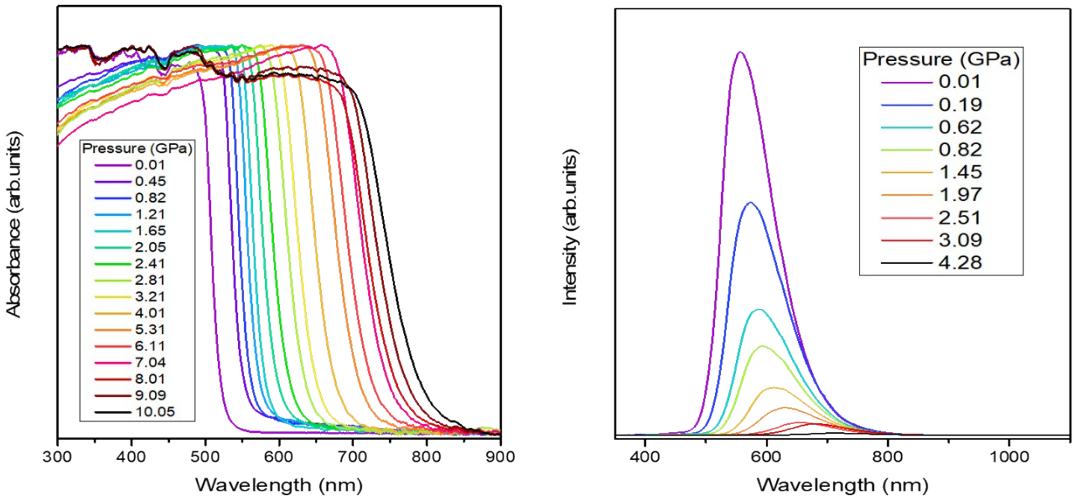

Figure S26. The situ absorption (left) and emisssion (right) spectra of 1-Y under different pressures. The emission color of the crystal gradually shifted from yellow (557nm) to red (684 nm), along with a monotonic decrease in intensity. The red shift was ascribed to the pressure-induced decrease of intermolecular distances and revolving of the molecular planes It was confirmed by the gradually broad and red-shifted absorption spectra with increment of pressure. The emission signal was fully quenched at the pressure of 4.28 GPa.

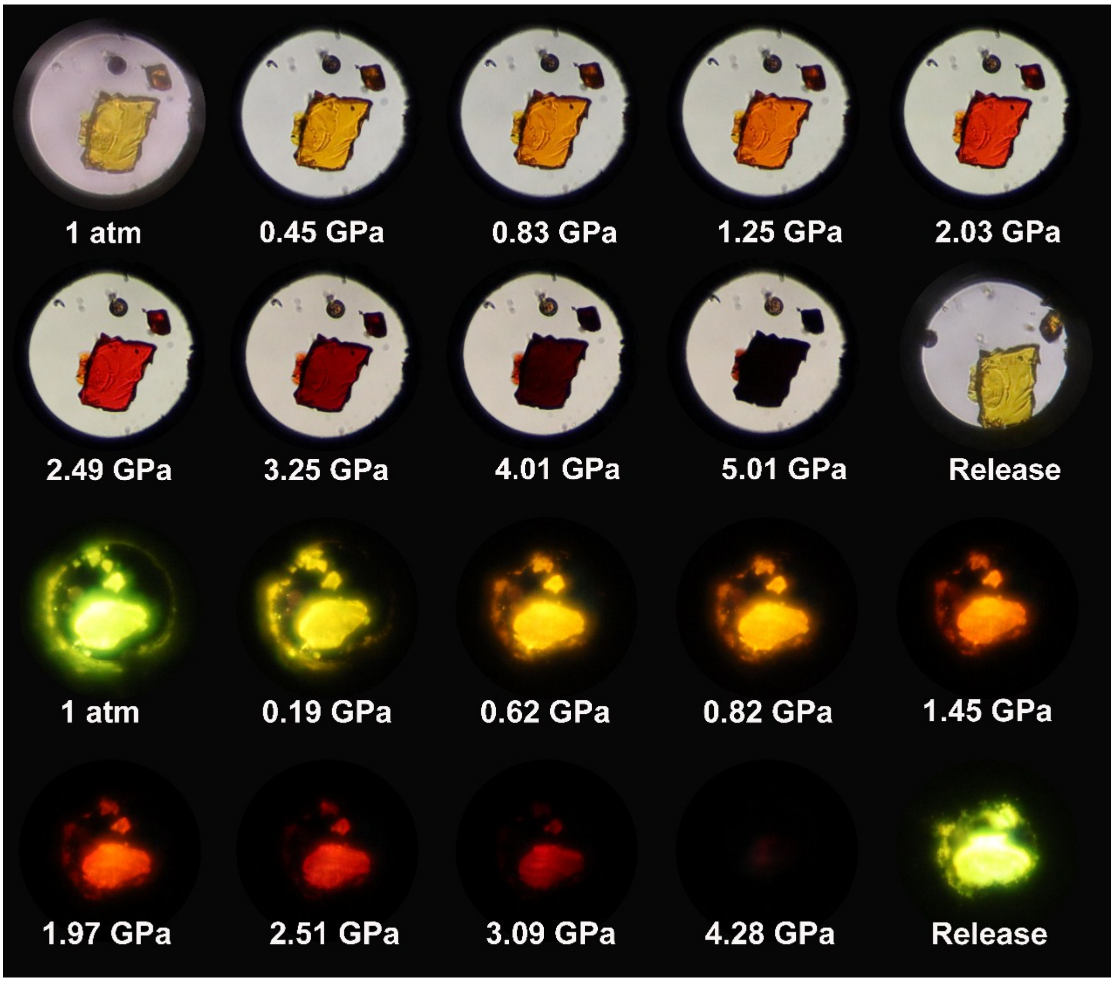

Figure S27. The situ absorption images (top) of 1-Y under different pressures under daylight, and the situ fluorescense images (bottom) of 1-Y under different pressures. The images were obtained using a camera (Canon Eos 5D mark Ⅱ) equipped on a microscope (Ecilipse TI-U, Nikon).The carema can record the photographs under the same conditions including exposure time and intensity.

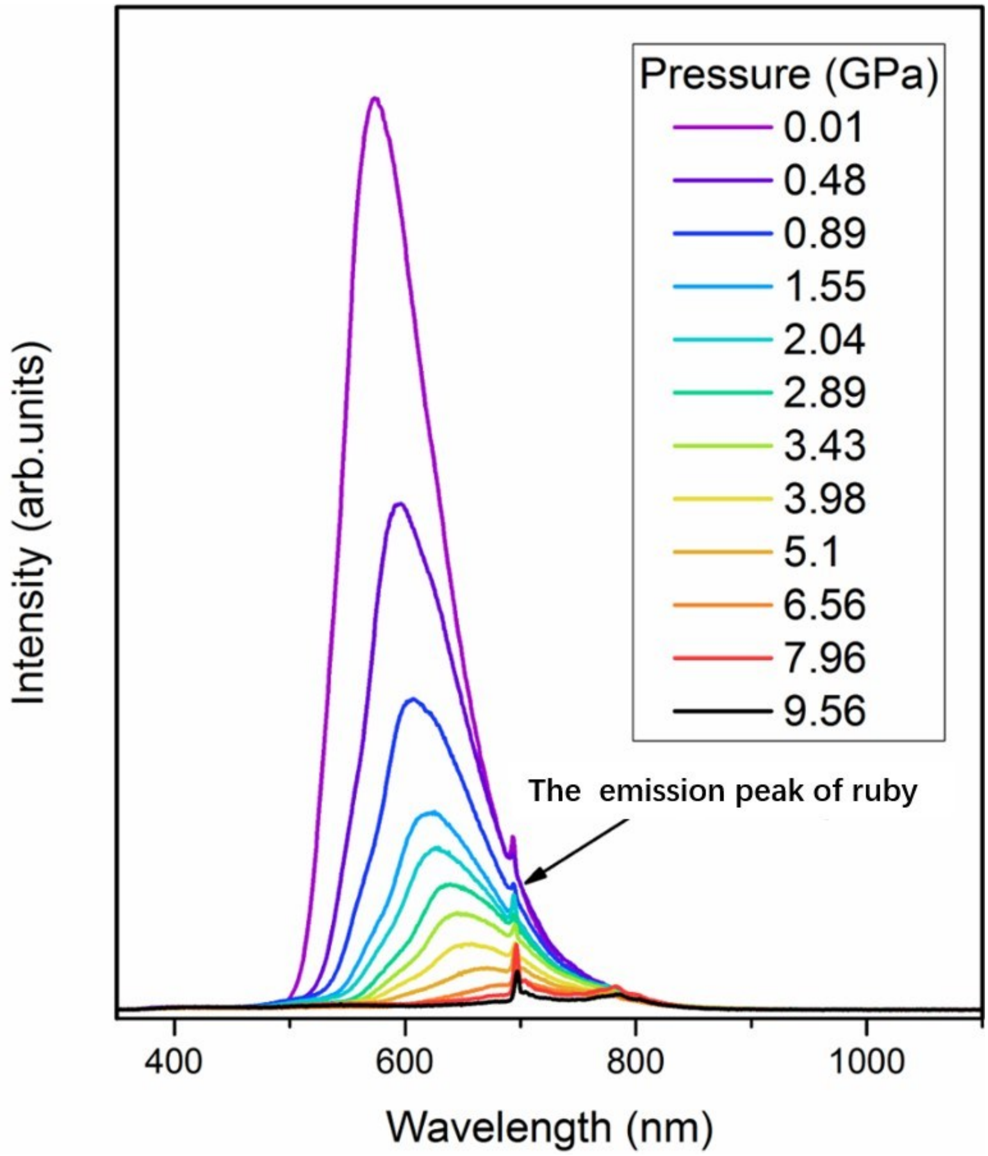

Figure S28. The situ emisssion spectrum of 1-O under different pressures. The emission color of the crystal gradually shifted from orange (580nm) to NIR (720 nm), along with a monotonic decrease in intensity. The emission signal was fully quenched at the pressure of 9.56 GPa.

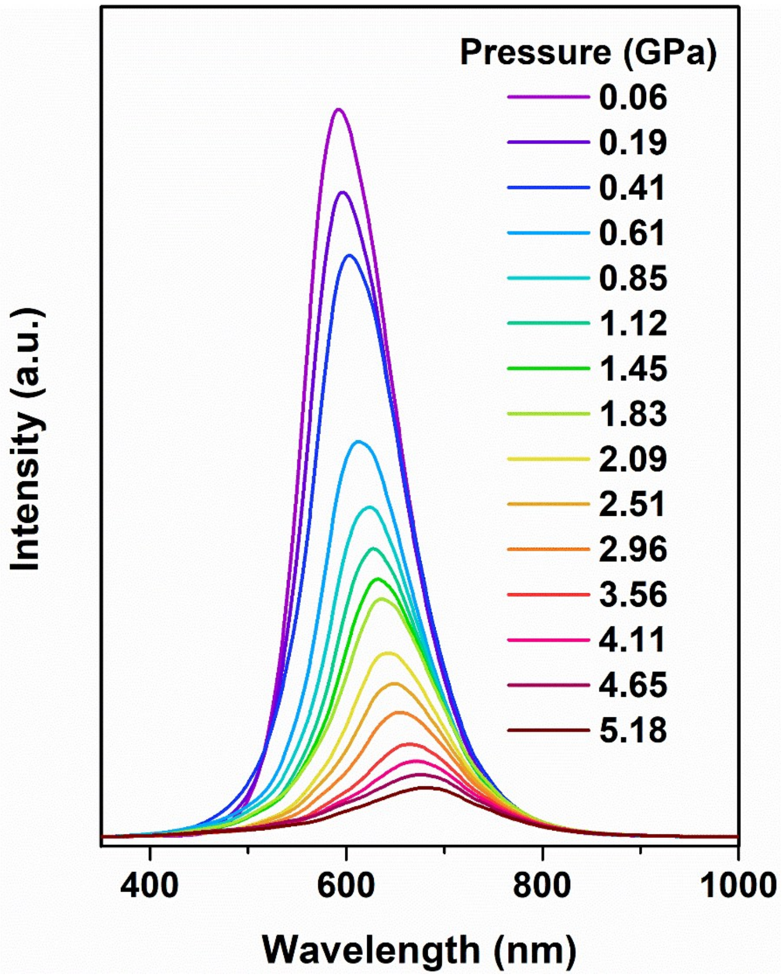

Figure S29. The situ emisssion spectrum of 1-R under different pressures. The emission color of the sample gradually shifted from red (618 nm) to NIR. The emission signal declined with the increase of the pressure. When compressed, the molecules would adjust their position in order to adapt to the smaller volume. The closer motion of molecules could ultimately lead to strengthening of intermolecular interactions and a red-shifted emission. On the other hand, the molecules became closer and the intermolecular interactions became stronger, which meant that the molecules revolved to more parallel. That promoted effective intermolecular π–π stacking interactions, which were responsible for the emission quenching.

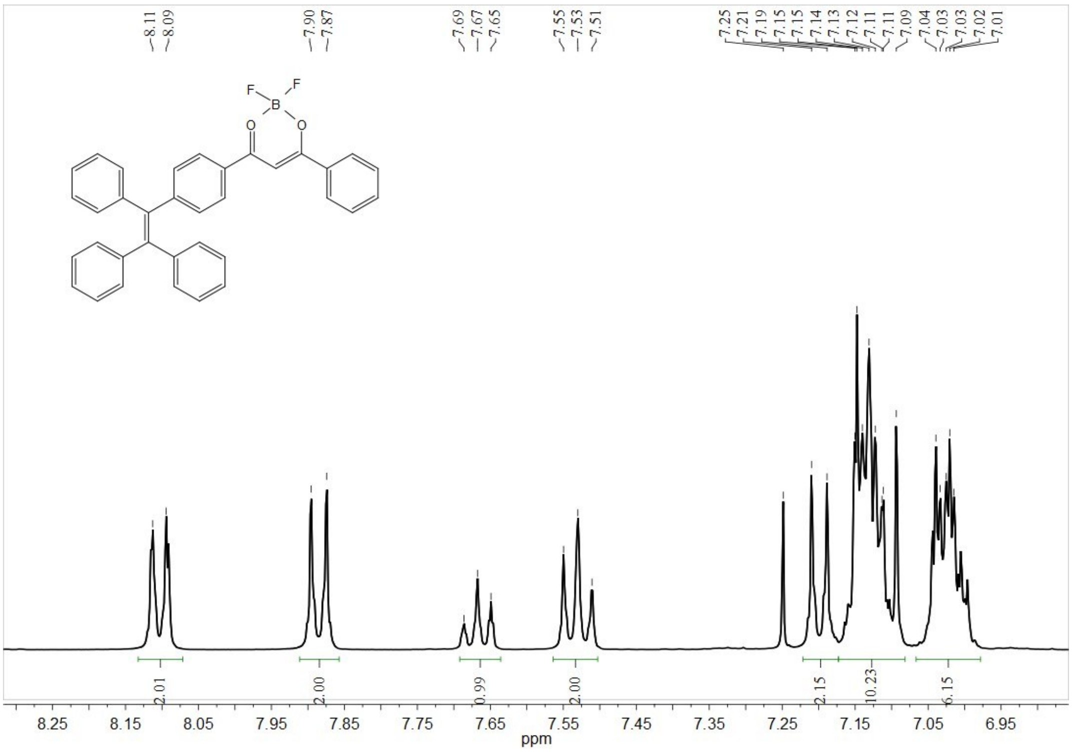

Figure S30. The ^{1}H NMR spectrum of compound **1** in CDCl$_3$. ^{1}H NMR (400 MHz, CDCl$_3$) δ 8.10 (d, *J* = 7.4 Hz, 2H), 7.89 (d, *J*= 8.5 Hz, 2H), 7.67 (t, *J* = 7.4 Hz, 1H), 7.53 (t, *J* = 7.8 Hz, 2H), 7.20 (d, *J* = 8.5 Hz, 2H), 7.17-7.09 (m, 10H), 7.06 -6.97 (m, 6H).

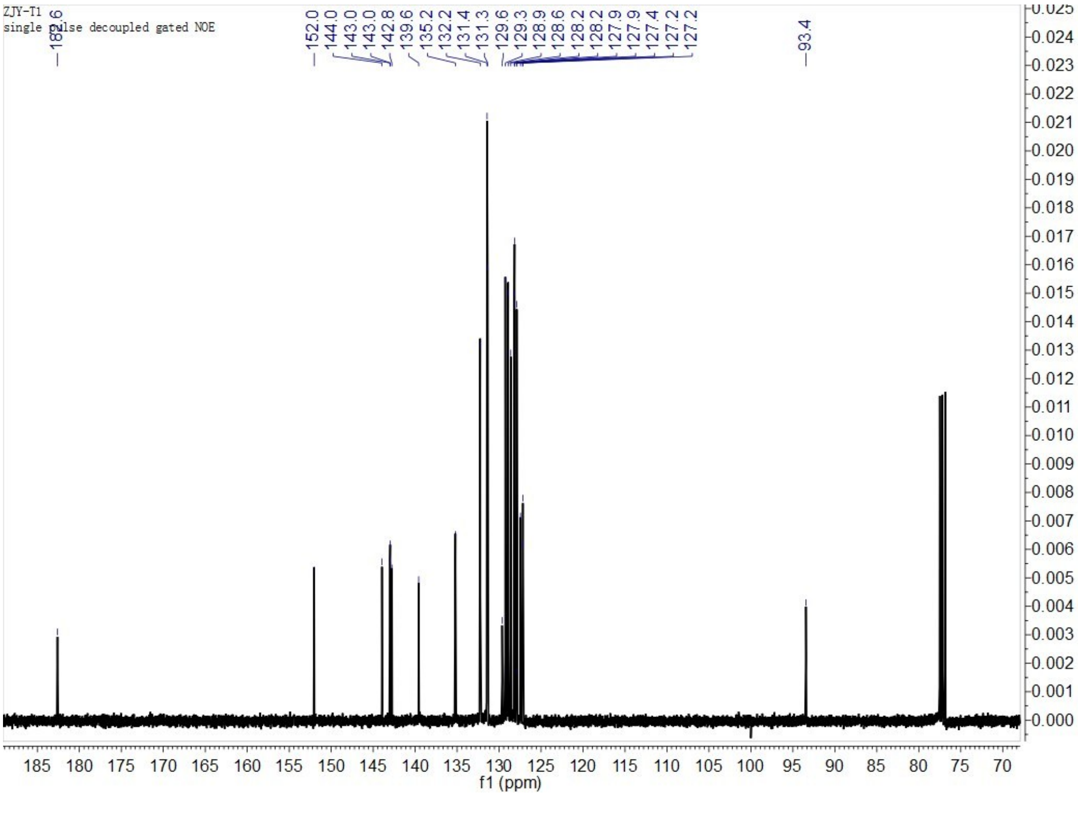

Figure S31. The ^{13}C NMR spectrum of compound **1** in CDCl$_3$. ^{13}C NMR (101 MHz, CDCl$_3$) δ 182.6, 152.0, 144.0, 143.0, 143.0, 142.8, 139.6, 135.2, 132.2, 131.4, 131.4, 129.6, 129.3, 128.9, 128.6, 128.2, 128.2, 127.9, 127.5, 127.2, 127.2, 93.4.

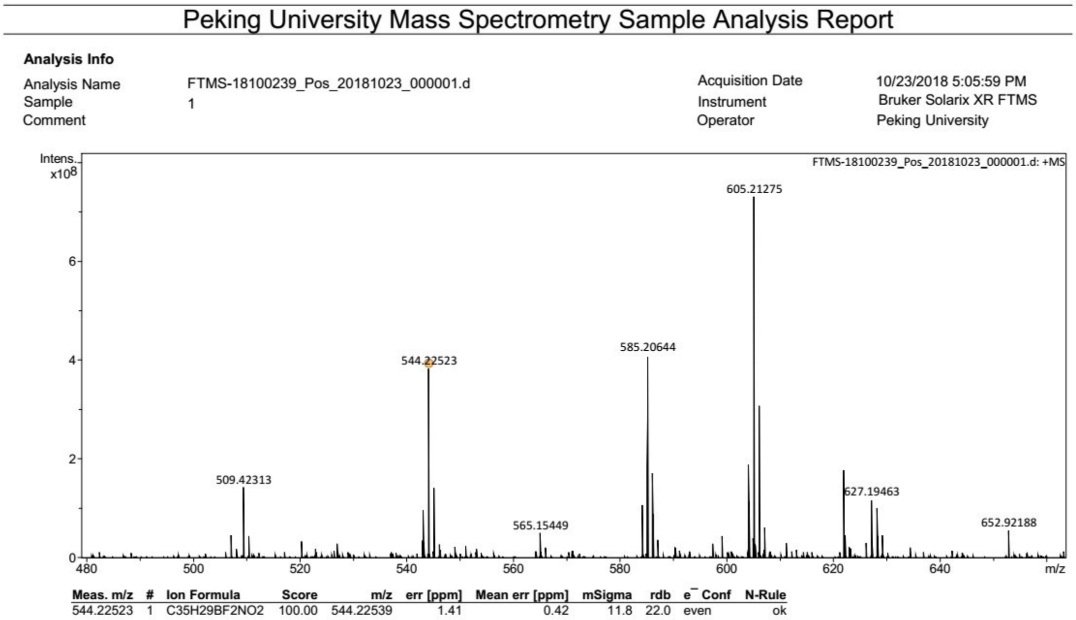

Peking University Mass Spectrometry Sample Analysis Report

Analysis Info

Analysis Name	FTMS-18100239_Pos_20181023_000001.d	Acquisition Date	10/23/2018 5:05:59 PM
Sample	1	Instrument	Bruker Solarix XR FTMS
Comment		Operator	Peking University

Meas. m/z	#	Ion Formula	Score	m/z	err [ppm]	Mean err [ppm]	mSigma	rdb	e¯ Conf	N-Rule
544.22523	1	C35H29BF2NO2	100.00	544.22539	1.41	0.42	11.8	22.0	even	ok

Figure S32. The HR-ESI spectrum of compound **1**.

References

(1) Chen, P.-Z.; Niu, L.-Y.; Chen, Y.-Z.; Yang, Q.-Z., Difluoroboron β-diketonate dyes: Spectroscopic properties and applications. *Coord. Chem. Rev.* **2017,** 350, 196-216.
(2) Qi, Y.; Wang, Y.; Yu, Y.; Liu, Z.; Zhang, Y.; Du, G.; Qi, Y., High-contrast mechanochromism and polymorphism-dependent fluorescence of difluoroboron β-diketonate complexes based on the effects of AIEE and halogen. *RSC Adv.* **2016,** 6, 33755-33762.
(3) Chen, P.-Z.; Wang, J.-X.; Niu, L.-Y.; Chen, Y.-Z.; Yang, Q.-Z., Carbazole-containing difluoroboron β-diketonate dyes: two-photon excited fluorescence in solution and grinding-induced blue-shifted emission in the solid state. *J. Mater. Chem. C.* **2017,** 5, 12538-12546.
(4) Zhai, L.; Zhang, F.; Sun, J.; Liu, M.; Sun, M.; Lu, R., New non-traditional organogelator of β-diketone-boron difluoride complexes with terminal tetraphenylethene: Self-assembling and fluorescent sensory properties towards amines. *Dyes Pigm.* **2017,** 145, 54-62.